Chapter 5

Forced Response: Laminar Flat Flame Burner

Since a large number of physical parameters influence the flame dynamics in a full scale gas turbine combustor, it is virtually impossible to develop physically correlated reduced order models for flame dynamics by directly studying these complex reacting flows. Even the Rijke tube combustor system, though comprising of a simple geometry and a flat flame, shows a strong nonlinear coupling between acoustics and the heat release rate of the flame. This coupling mechanism can not be understood or analyzed by continuing to investigate the reacting flow in the Rijke tube combustor. A first step in understanding the dynamics of complex flames seen in gas turbines is by performing linear stability analysis of a flame in a simple geometry, such as a planar flame.

5.1 Rationale and Objectives

Having started with a simple system which has a lower number of physical variables affecting the flame dynamics, physically co-related reduced order models can be built. These reduced

order models could then be expanded upon by adding complexities to the combustion process. With this idea in mind, it was decided to numerically study the dynamic response of a premixed laminar flat flame (similar to the one modeled in the Rijke tube combustor study – see chapter 4) due to controlled velocity perturbations imparted on the reactants. This study has been formulated to understand the effects of flame speed oscillations and chemical kinetics on the flame dynamics. From literature, it is observed that the flames normally respond as a low pass filter to acoustic perturbations [67]. Considering this, the present study was limited to a frequency bandwidth of 20-300 Hz.

The linear stability of premixed flames dates back to the Landau–Darrieus analysis (Landau and Lifshitz [68]), which treats the flame as a discontinuity that separates inert hydrodynamic flows. In later studies, high activation temperature asymptotic analyses were employed, in which the reaction zone is still treated as a discontinuity (the 'flame sheet') but the structure of the diffusive preheat zone is taken into account. Sivashinsky [69] used the constant density approximation (CDA), which completely ignores hydrodynamic effects and is formally valid in the limit of small heat release. He showed that for Lewis numbers (ratio of thermal to species diffusivities) sufficiently less than unity, thermal-diffusive effects alone are sufficient to cause the cellular instability. He also found a pulsating instability for Lewis numbers sufficiently above unity. Joulin and Clavin [70], Buckmaster [71] and Jackson and Kapila [72] showed that large enough heat losses can make premixed flames unstable to the pulsating instability. Frankel and Sivashinsky [73], Matalon and Matkowsky [74] and Pelce and Clavin [75] performed slowly-varying flame (SVF) analyses in which the wavelength of the perturbation is assumed to be much longer than the flame thickness

More recently linear stability analyses have been performed using numerical methods for finite activation temperatures, in which the full structure, including that of the reaction zone of the flame is taken into account. Mukunda and Drummond [76] used a spectral collocation scheme with a simple model for hydrogen–oxygen involving four species and variable transport properties. Liberman et al. [77] examined the problem using a shooting method, ignoring viscosity and used unity Lewis number, and hence did not take into account

thermal-diffusive effects. Lasseigne et al. [78] used the CDA model with finite activation temperature, which ignores the hydrodynamics.

In a recent study by Sharpe [79], linear stability of freely propagating planar steady premixed flame was investigated by solving the full reacting Navier–Stokes equations, for different parameters (activation temperature, Lewis number, heat release, Prandtl number and wavenumber of disturbance). There are several reasons for performing analyses with finite activation temperatures. First, one does not know from an asymptotic analysis how high the activation temperature has to be for the results to be quantitatively or even qualitatively correct, only that the predictions of the analysis become better as the activation temperature tends to infinity. For the CDA model Lasseigne et al. [78] found that the infinite activation temperature results of Sivashinsky [69] were at best only qualitatively correct for realistic, but finite activation temperatures.

Hence, it is important to check the validity of the asymptotic linear stability results, and also the validity of the other asymptotic approximations made (the limits of small heat release in the CDA analysis and small wavenumber in the SVF analysis), for realistic parameter values. Also, the high activation temperature asymptotic results mentioned above all assume that the Lewis number is asymptotically close to one, i.e. near-equidiffusional flames (NEFs). However, the Lewis number can vary between about 0.3 for hydrogen to 1.8 for propane, and hence a method is required for determining the stability of flames with Lewis numbers $O(1)$ different from unity.

Kurdyumov and Fernandez-Tarrazo [80] investigated the propagation of premixed laminar flames with different Lewis numbers in open ducts of circular cross-section numerically with a thermal-diffusive model. Ducts with adiabatic and cold isothermal walls were considered. Recently, Boury and Joulin [81] studied the nonlinear dynamics of a premixed gaseous flame with a significant gas flow velocity $u_{||}$ existing parallel to the front. The chosen $u_{||}$ noticeably exceeded the critical value u_c corresponding to the transition between absolute and convective instability, whereby an external forcing was needed to trigger some wrinkling in the long-time

limit. The selected excitation was spatially localized and evolved randomly in time.

Day and Bell [82] developed an adaptive algorithm for low Mach number reacting flows with complex chemistry. The approach used a form of the low Mach number equations that discretely conserves both mass and energy. For a co-flowing methane/air diffusion flame the adaptive algorithm correctly predicted the experimentally observed flame lift-off height for both steady and time-dependent inlet gas flows, but required a restrictive numerical time step. McIntosh et al. [42] have studied pressure interactions with flat flames. They have developed a mathematical model to study pressure interactions with premixed flames in a prescribed strained velocity field. A stability analysis was carried out including pressure disturbances and an approximate frequency condition obtained. For positive strain the unsteady analysis indicated that the pulsating instability is suppressed.

To the knowledge of the author, there have not been many CFD studies with laminar flat flames that have concentrated on investigating the effects of mass flow rate perturbations on the heat release response of the flame by applying linear stability analysis. Perhaps the most comprehensive CFD modeling effort toward understanding the response of burner-stabilized flat flames to velocity perturbations has been conducted by Rook et al. [83]. The response of burner-stabilized flat flames to acoustic velocity perturbations was studied numerically and analytically although a stability analysis was not performed. The numerical setup involved the set of one-dimensional transport equations for low-Mach number reacting flow using both a simple and a complex reaction mechanism. An analytical model was also developed. Relations for the fluctuating heat release and heat loss to the burner were derived, from which the coupling between the velocity fluctuations at both sides of the flame was found.

Another one-dimensional study on the effects of velocity perturbations on flat flames has been carried out at VACCG by Haber [84]. The study was conducted to correlate the unsteady heat release from the flame to the OH^* chemiluminescence measurements obtained from experimental studies [85]. Premixed methane-air flow was numerically modeled using a modified PREMIX code [86]. Heat losses from the flame to the honeycomb and the ambient

were modeled and the GRIMECH detailed chemical mechanism [87] was used.

The present study is an improvement over computational studies that have been carried out in the past. The differences between the past studies and the current study is in the treatment of the heat transfer mechanisms. In particular, empirical modeling of heat transfer processes as followed by Haber [84] has been avoided as much as possible. Instead, two dimensional axisymmetric Navier-Stokes equations have been solved along with the full energy equation and species transport equations and only radiation modeling has been incorporated. The ultimate goal is to build on the laminar flame dynamics results and finally investigate turbulent swirl stabilized flames in full scale gas turbines. Therefore, it is important that the flat flame simulations be carried out at flame temperatures close to those seen in full-scale gas turbines.

5.2 Technical Approach

Normally, laminar flat flames are stabilized by losing a significant amount of energy to the flame holder that acts as a heat sink. Flames stabilized over such heat sinks are cool flames with flame temperatures almost 50% to 75% of the corresponding adiabatic flame temperatures. The need is to stay as close to gas turbine temperatures, yet simulate non-adiabatic laminar flat flames.

5.2.1 Energy Flow Description

Achieving temperatures close to observed gas turbine combustion maximum temperature is possible by applying the concept of excess enthalpy flames. The flame stabilizer plays the role of a heat exchanger rather than a heat sink and re-circulates most of the energy it draws from the flame front by heating up the incoming reactants (similar to the preheating of reactants seen in the Rijke tube. See Section 4.5.1). Thus, the flame is stabilized not by significantly

lowering the laminar flame speed but by increasing the speed of the reactants entering the flame front. The thermal loses from the flame front to the environment and from the flame stabilizer to the environment ensure that a non-adiabatic burning condition is achieved. A ceramic honeycomb flame stabilizer (similar to the one shown in Figure 4.3), which has a high percentage of volumetric porosity, is used to stabilize the flame. The selection of the honeycomb material helps fulfill the requirement of keeping the flame temperatures high.

5.2.2 Linear Stability Analysis

Linear stability analysis of the flat flame has been carried out by 'forcing' (perturbing) the flame with incoming mass flow oscillations. Sinusoidal inlet velocity boundary condition has been applied to generate open-loop Frequency Response Functions (FRF), which in turn are to facilitate the prediction of close-loop behavior for a self-excited system like the Rijke tube combustor (see Chapter 4).

Frequency Response Function

The frequency response of a system can be viewed in two different ways: via the Bode plot or via the Nyquist diagram. Both methods display the same information; the difference lies in the way the information is presented. The frequency response is a representation of the system's response to sinusoidal inputs at varying frequencies. The output of a linear system to a sinusoidal input is a sinusoid of the same frequency but with a different magnitude and phase. The frequency response is defined as the magnitude and phase differences between the input and output sinusoids. We can use the open-loop frequency response of a system to predict its behavior in closed-loop.

To plot the frequency response, a vector of frequencies (varying between zero or 'DC' and infinity) is created and the value of the plant transfer function is computed at those frequencies. If $G(s)$ is the open loop transfer function of a system and ω is the frequency vector,

$G(j\omega)$ vs. ω is then plotted. Since $G(j\omega)$ is a complex number, both its magnitude and phase can be plotted (the **Bode plot**) or its position in the complex plane is plotted (the Nyquist plot) . A Bode plot is the representation of the magnitude and phase of $G(j\omega)$ (where the frequency vector ω contains only positive frequencies). Figure 5.1 displays the Bode plots for the transfer function:

$$G(s) = \frac{50}{s^3 + 9s^2 + 30s + 40} \tag{5.1}$$

The frequency is on a logarithmic scale, the phase is given in degrees, and the magnitude is given as the gain in decibels. A decibel is defined as $20 \log_{10}(|G(j\omega)|)$. The FRF calculations in this study have been performed using a MATLAB code (see Appendix C).

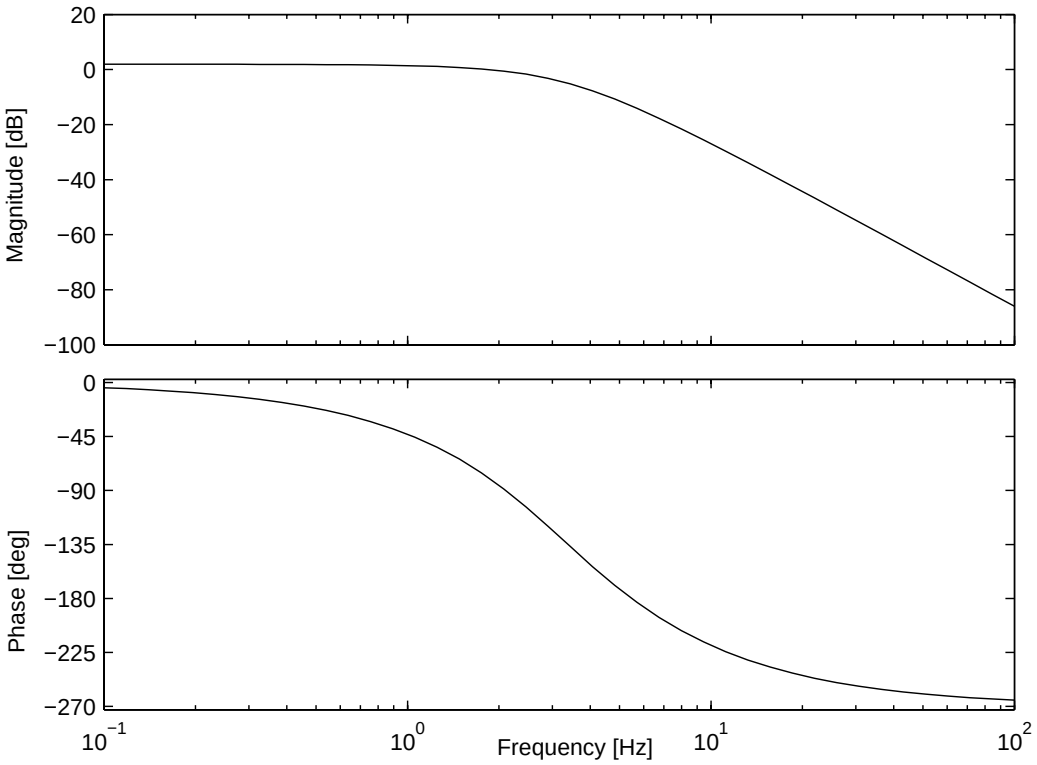

Figure 5.1: Bode plot for the transfer function $G(s) = \frac{50}{s^3+9s^2+30s+40}$

Gain and Phase Margin

Consider the system shown in Figure 5.2. In the system, K is a variable (constant) gain and $G(s)$ is the plant under consideration. The **gain margin** is defined as the change in open loop gain required to make the system unstable. Systems with greater gain margins can withstand greater changes in system parameters before becoming unstable in closed loop. The **phase margin** is defined as the change in open loop phase shift required to make a closed loop system unstable.

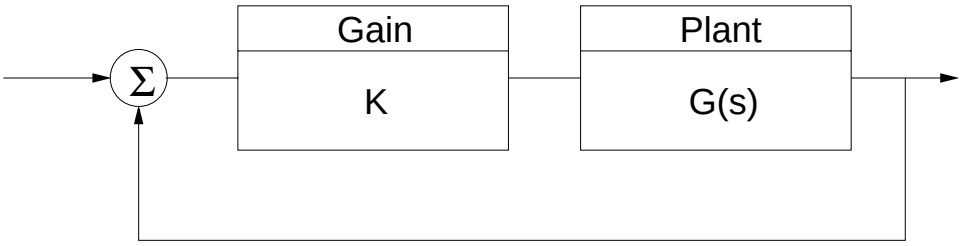

Figure 5.2: Sketch of a control system represented in block diagram form

The phase margin also measures the system's tolerance to time delay (t_d). If there is a time delay greater than $180/\omega_{pc}$ in the loop (where ω_{pc} is the frequency where the phase shift is 180°), the system will become unstable in closed loop. The time delay can be thought of as an extra block in the forward path of the block diagram that adds phase to the system but has no effect on the gain. That is, a time delay can be represented as a block with magnitude of 1 and phase $\omega \times t_d$ (in rad/s). The phase margin is the difference in phase between the phase curve and $-180°$ at the point corresponding to the frequency that gives us a gain of $0\,dB$ (the gain cross over frequency, ω_{gc}). Likewise, the gain margin is the difference between the magnitude curve and $0\,dB$ at the point corresponding to the frequency that gives us a phase of $-180°$ (the phase cross over frequency, ω_{pc}).

Bandwidth Frequency

The bandwidth frequency is defined as the frequency at which the closed-loop magnitude response is equal to $-3\,dB$. However, when the design is via frequency response, the interest is in predicting the closed-loop behavior from the open-loop response. Therefore, a second-order system approximation will be used and it can be said that the bandwidth frequency equals the frequency at which the open-loop magnitude response is between $-6\,dB$ and $-7.5\,dB$, assuming the open loop phase response is between $-135°$ and $-225°$. Inputs with frequency less than ω_{bw} (the bandwidth frequency) are tracked reasonably well by the system. Sinusoidal inputs with frequency greater than ω_{bw} are attenuated (in magnitude) by a factor of 0.707 or greater (and are also shifted in phase).

Closed-loop performance

In order to predict closed-loop performance from open-loop frequency response, we need to ensure the following criteria are met:

- The system must be stable in open loop if we are going to design via Bode plots.
- If the gain cross over frequency is less than the phase cross over frequency ($\omega_{gc} < \omega_{pc}$), then the closed-loop system will be stable.
- For second-order systems, the closed-loop damping ratio is approximately equal to the phase margin divided by 100 if the phase margin is between 0° and 60°. We can use this concept with caution if the phase margin is greater than 60°.
- A very rough estimate is that the bandwidth is approximately equal to the natural frequency.

5.2.3 Flow Forcing Techniques

Using sinusoidally varying velocity at the inlet to perturb the flame is called 'flow forcing'. There is considerable reduction of computation time (compared to self-excited combustor simulation) when flow forcing is applied to a flame. The reduction takes place because flow forcing can be applied by considering only a part of the total combustor geometry. In our case, the upstream part of the flat flame burner need not be considered and only the flame region need be considered (see Figure 5.3).

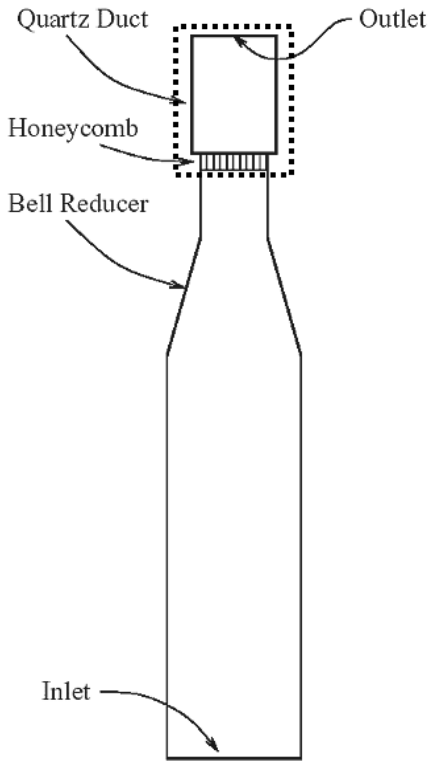

Figure 5.3: Internal geometry of the flat flame burner showing the computational domain required for the flow forcing study

Two forcing techniques have been described by Kaufmann et al. [88] – the inlet wave modulation method (IWM) and the inlet velocity modulation method (IVM).

Inlet Wave Modulation Method

This forcing technique modulates the wave entering the chamber while letting the wave leaving the domain propagate without reflection at the computational inlet. The basic idea is to impose A^+, the amplitude of the wave entering the computational domain. To apply the IWM method to CFD codes, boundary conditions based on methods of characteristic [13, 89, 90] must be used.

Inlet Velocity Modulation Method

In IVM, a fluctuating velocity is imposed at the inlet section. The inlet velocity has the form:

$$u(x_0, t) = \overline{u} + u'(x_0, t) \tag{5.2}$$

where $\overline{u}$ is the mean velocity and $u'(x_0, t)$ is the imposed fluctuation:

$$u'(x_0, t) = u_0 \exp^{-i\omega t} \tag{5.3}$$

In the linear regime, this boundary condition is representative of a loudspeaker whose membrane moves with the amplitude u_0/ω. As long as flow forcing is not carried out near the eigenfrequencies of the chamber, this method remains a safe option.

5.3 Accompanying Experimental Studies

The experimental setup used for the study is schematically shown in Figure 5.4. The system consisted of mass flow meters, a mixing chamber that thoroughly mixed the oxidizer and the fuel prior to their injection into the laminar flat flame burner where a flat flame was stabilized using a ceramic honeycomb. Thermocouples embedded in the top and bottom surface of the honeycomb monitored its temperature, while two microphones were used to measure the effective velocity perturbations. Controlled velocity perturbations were imparted using a 5″,

$60\,W$, $8\,\Omega$ speaker. OH^* signal measured from the top of the burner using a monochrometer and a photomultiplier tube (PMT) was taken to be the measure of the dynamic heat release rate. The dynamic signals and the flow parameters were recorded using a data acquisition system.

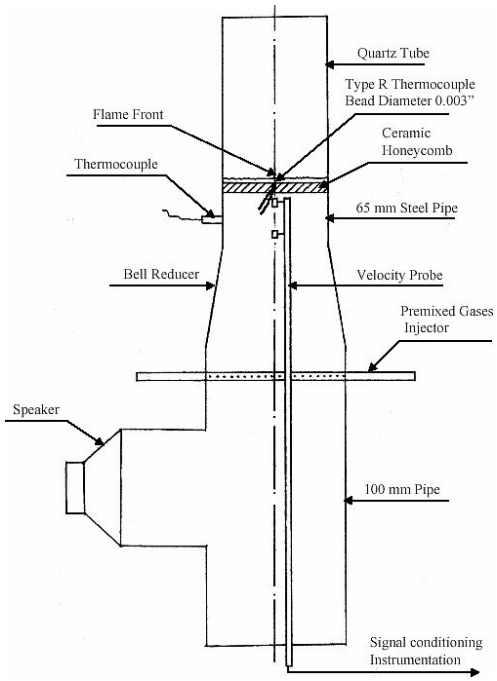

Figure 5.4: Flat flame burner experimental setup

Experiments were conducted with bottled instrument grade methane as fuel for five equivalence ratios ranging from 0.5 to 0.75, and four flow rates ranging from $145\,cc/s$ to $200\,cc/s$. Figure 5.5 and Figure 5.6 show the magnitude and phase, respectively, of the FRF between the OH^* chemiluminescence signal (output) and the velocity fluctuations (u', input) for $145\,cc/s$. Figure 5.5 details the magnitude of the FRF. We can observe that for the test conditions studied, there are two clearly visible damped resonant peaks, indicating that the FRF is fourth order in nature. The two resonances are clearly seen at higher equivalence ratios (ϕ), while at lower ϕ they are at frequencies very close to one another making it difficult to visualize and identify their presence. The FRF (magnitude) plot indicates that for changes in

ϕ and for a fixed Q_{total}, the frequency of the 1st resonant response varies between 25 Hz and 40 Hz. With an increase in ϕ, the peak of the 1st resonant response becomes less pronounced indicating an increase in its damping. Therefore, at the lower end of the frequency range, an increase in ϕ causes a reduction in the FRF magnitude (also termed as the dynamic gain of the transfer function). This character of the 1st resonant response is exhibited at all the flow rates studied. The frequency of the 2nd resonant response increases significantly with increasing ϕ, for all the total flow rates studied. This movement of the frequency of the 2nd resonant response is primarily responsible for broadening of the bandwidth of the FRF, which leads to higher FRF magnitudes at the upper end of the investigated frequency range. Based on the above discussion, it can be concluded that an increase in ϕ adds damping at lower frequencies, and broadens the bandwidth of the flame dynamic response.

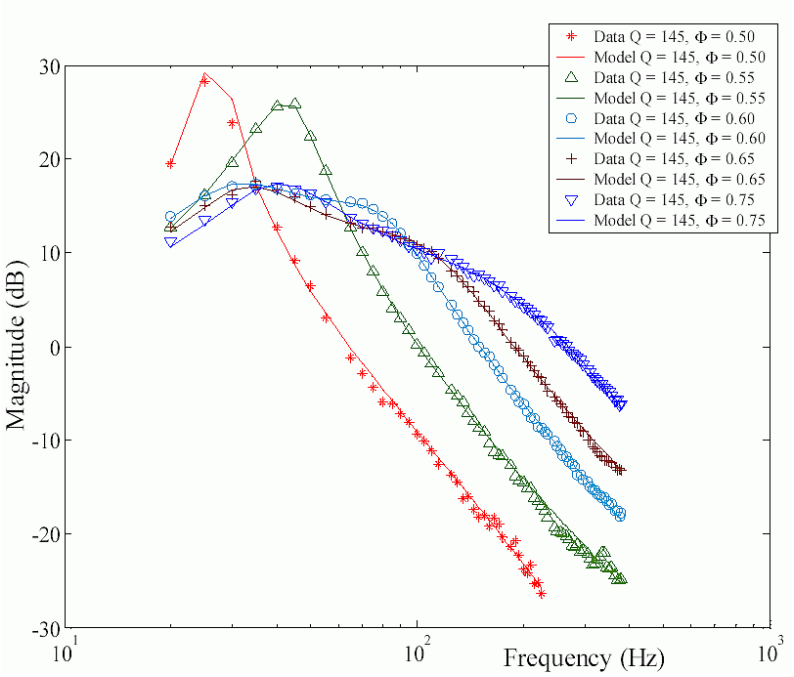

Figure 5.5: Experimental FRF magnitude for the flat flame ($Q = 145\, cc/s$)

Figure 5.6 shows the phase of the FRF. The plot shows that for lower values of ϕ, there is a sharp drop in the phase at frequencies associated with the range of 1st resonant response;

beyond which the drop in phase is less pronounced. This behavior indicates the presence of lightly damped resonances at the low frequency range and no significant dynamic activity, due to lack of resonances at higher frequencies. With an increase in ϕ, the magnitude of the drop in phase around the lower frequency range is diminished which points to an increase in damping of the 1st resonant response. Increase in ϕ also decreases the drop in phase over the entire frequency range investigated. This indicates a broadening of the bandwidth, which has been attributed to the movement of the 2nd resonant response to higher frequencies. At any particular fixed frequency of interest, within the range of 35-380 Hz, it was observed that an increase in ϕ changed the phase of the FRF significantly. The change in phase is most pronounced in the frequency range of 35-100 Hz. This observation can aid in the successful implementation of active control methodologies that are based on fluctuation in ϕ.

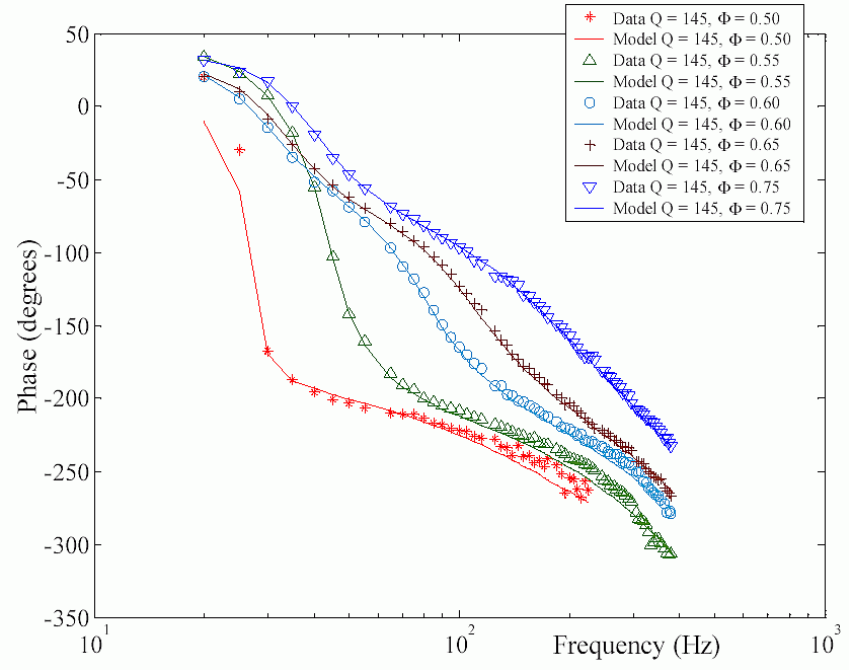

Figure 5.6: Experimental FRF phase for the flat flame ($Q = 145\, cc/s$)

5.4 Computational Model

A two-dimensional representation of the region of interest (shown in Figure 5.3 and henceforth referred to as 'computational domain') in the flat flame burner has been selected for the simulation. The computational domain is illustrated in Figure 5.7. The honeycomb is positioned $1\,cm$ downstream of the computational inlet. The outlet, quartz wall of the burner and the symmetry axis are also shown.

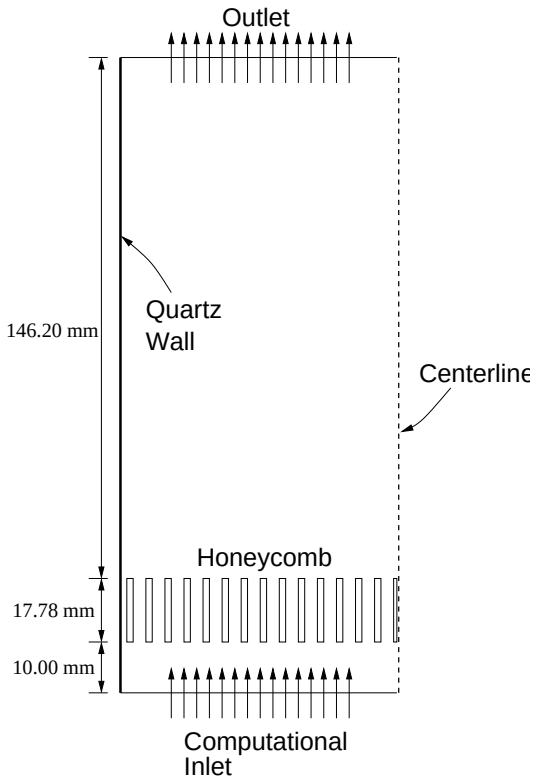

Figure 5.7: Flat flame burner computational domain (not to scale)

5.4.1 Grid Generation

The grid has been generated using structured quadrilateral (quad) and unstructured triangular (tri) cells following a similar method first implemented in the Rijke tube simulation

(see Section 4.4). Figure 5.8 shows the closeup of the honeycomb, flame region and the downstream sections of the grid. The grid is structured (quad) upstream of the honeycomb as well as inside the honeycomb channels. Downstream of the honeycomb is the flame region where initially a coarse tri grid was initially generated. After the initial steady state solution was achieved, the flame region grid was adapted to improve its resolution. The flame shape at steady state can be seen downstream of the honeycomb exit. Beyond the flame region a coarser tri grid was generated. Further downstream the grid changes back to structured quad cells.

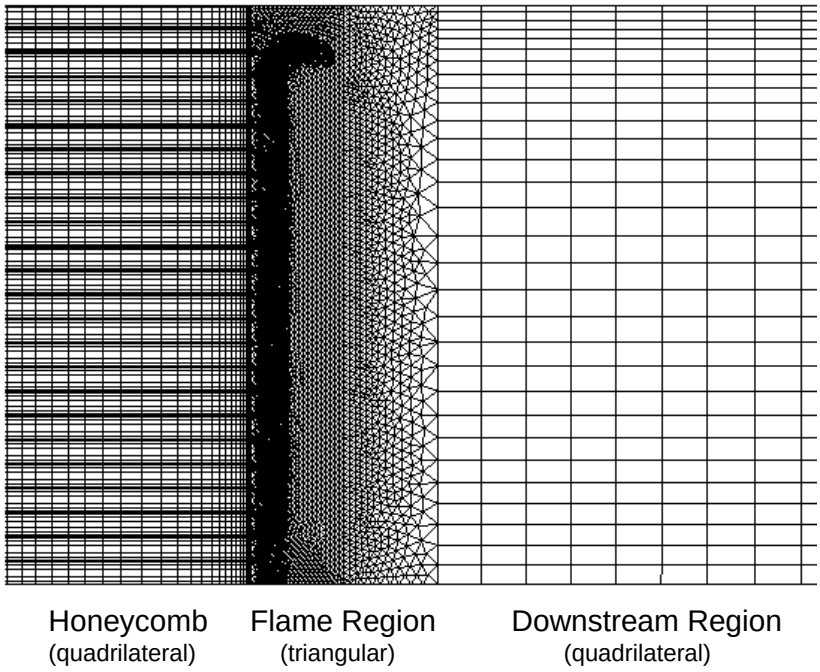

Figure 5.8: Flat flame burner grid showing the honeycomb, flame and downstream regions

5.4.2 Flow Modeling

Similar to the Rijke tube simulation, the segregated solver of Fluent has been used for simulating the flow in the flat flame burner geometry. Second order accurate schemes for

velocities, species and energy have been implemented. A second-order accurate scheme has been used for pressure interpolation and the SIMPLE algorithm has been chosen for pressure-velocity coupling. Instead of the PISO algorithm, which was used in the Rijke tube combustor simulation, SIMPLE has been chosen. This is because even though the PISO scheme results in faster convergence of the solution for every time-step, the inherent advantage of using the PISO scheme lies in its ability to incorporate skewness correction to unstructured triangular cells which have high equiangular skewness [63]. Since quadrilateral structured grid has been used in the flat flame combustor computational domain, using PISO for pressure-velocity correction will not lead to any additional convergence acceleration.

5.4.3 Chemistry and Heat Transfer Modeling

It was observed in the Rijke tube combustor study that the single-step mechanism (see section 4.4.3) caused a computationally 'stiff'[1] set of differential equations. Although, the number of species in a two-step mechanism is higher by one (CO is the extra specie), but the slightly higher computational requirement is offset by the relative reduction in stiffness. Therefore, the two-step reaction mechanism [59] shown below has been used for the simulation.

$$CH_4 + \frac{3}{2}O_2 \rightarrow CO + 2H_2O \tag{5.4}$$

$$CO + \frac{1}{2}O_2 \rightarrow CO_2 \tag{5.5}$$

$$CO_2 \rightarrow CO + \frac{1}{2}O_2 \tag{5.6}$$

[1] A network of equations is stiff if the eigenvalues of the coefficient matrix of its locally linear representation have negative real parts that are widely disparate. Therefore, to be classified as 'stiff', a network of equations must have eigenvalues which are both widely separated and mostly real and negative. Stiff behavior is found in nearly all aspects of combustion modeling. Kee and Dwyer [91] have reviewed stiffness in combustion models in detail.

where the reaction rates (in $kmol/m^3$-s) are expressed as:

$$\frac{d[CH_4]}{dt} = -A_{5.4} \exp\left(\frac{-E_{a,5.4}}{R_u T}\right) [CH_4]^{m_{5.4}} [O_2]^{n_{5.4}} \quad (5.7)$$

$$\frac{d[CO]}{dt} = -A_{5.5} \exp\left(\frac{-E_{a,5.5}}{R_u T}\right) [CO]^{m_{5.5}} [O_2]^{n_{5.5}} [H_2O]^{p_{5.5}} \quad (5.8)$$

$$\frac{d[CO_2]}{dt} = -A_{5.6} \exp\left(\frac{-E_{a,5.6}}{R_u T}\right) [CO_2]^{m_{5.6}} \quad (5.9)$$

The constants A, m, n, p and E_a $(J/kgmol)$ for each reaction are given in Table 5.1 (Taken from [59]).

Table 5.1: Constants for two-step global mechanism for CH_4 oxidation

Rate eqn.	Eqn. 5.4	Eqn. 5.5	Eqn. 5.6
A	5.012×10^{11}	2.239×10^{12}	5×10^8
E_a	2×10^8	1.7×10^8	1.7×10^8
m	0.7	1	1
n	1.5	0.5	–
p	–	0.5	–

Radiative heat transfer modeling has been implemented by using the Discrete Ordinates (DO) model. The DO radiation model solves the radiative transfer equation (RTE) [92] for a finite number of discrete solid angles, each associated with a vector direction $\vec{s}$ fixed in the global Cartesian system (x, y, z). The fineness of the angular discretization is user controlled, analogous to choosing the number of rays for ray tracing models. Unlike the ray tracing models, the DO model does not perform ray tracing. Instead, the DO model transforms the RTE into a transport equation for radiation intensity in the spatial coordinates (x, y, z). The DO model solves for as many transport equations as there are directions $\vec{s}$. The solution method is identical to that used for fluid flow and energy equations. The DO model works across the range of optical thicknesses, but is substantially more expensive to use compared to other simpler models. Since the optical thickness of the medium was not estimated

during the course of the investigation, it was safe to use the DO model that could model both optically thick as well as thin media. The burner wall was made of quartz (a semi-transparent medium) therefore the DO model was a good choice since only the DO model allows specular reflection and calculation of radiation in semi-transparent media.

5.4.4 Boundary and Initial Conditions

The IVM method has been applied to perturb the laminar flat flame. The inlet boundary is subjected to time-varying sinusoidal velocity. The mean value ($\overline{u}$) is imposed along with the sinusoidally fluctuating component (u'), and the instantaneous velocity, at a given time (t) and for a frequency of excitation (ω), is computed as:

$$u = \overline{u}\,[1 + 0.1\sin(2\pi\omega t)] \tag{5.10}$$

where, $u' = 0.1\overline{u}\sin(2\pi\omega t)$. The outlet boundary is at atmospheric pressure ($p' = 0$). The outside surface of the quartz wall is assumed to convect heat to the ambient and a heat transfer coefficient of $5\,W/m^2K$ has been imposed. Boundary conditions implemented are summarized in Table 5.2.

Table 5.2: Boundary conditions for the flat flame burner simulation

Boundary	Boundary Condition
Computational Inlet	Uniform velocity profile with imposed u' sinusoidal oscillations from $20\,Hz$ to $300\,Hz$
Outlet (Open)	Atmospheric pressure ($p' = 0$)
Burner wall	Convective heat loss to the ambient from the outer wall
Honeycomb walls	Coupled to the adjoining solid and fluid regions

The steady state solution was first achieved by igniting the air-fuel mixture using a high temperature patch downstream of the honeycomb flame stabilizer. An initial condition of cold flow was established before the ignition was initiated.

5.5 Results and Discussion

Results from the CFD study of the flat flame burner are being presented in this section. A flow rate of $Q = 200\,cc/s$ and equivalence ratio of $\phi = 0.75$ were chosen for the study. Steady state results from the simulations will be first highlighted followed by the dynamic results.

5.5.1 Reacting Flowfield Structure

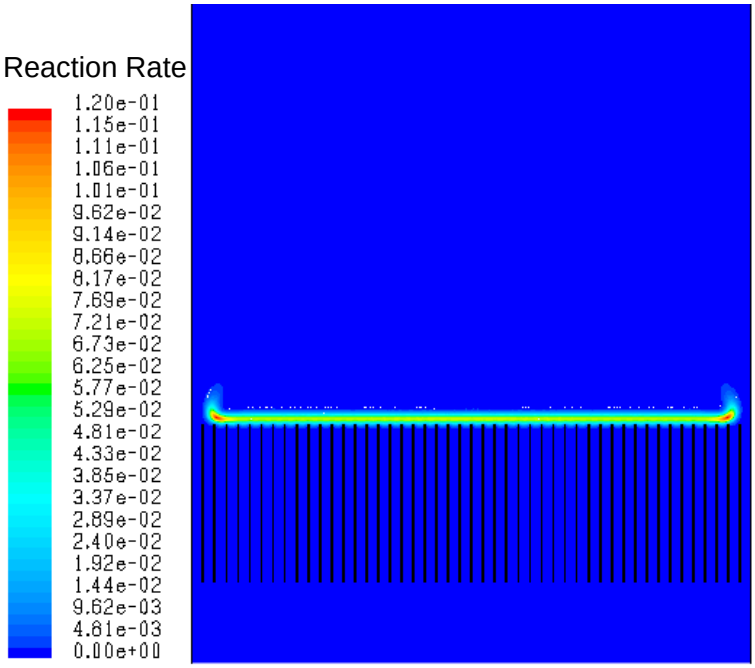

Figure 5.9: Flame anchored on top of the honeycomb seen in the form of reaction rate contours inside the flat flame burner

Steady state results of the $Q = 200\,cc/s$ and $\phi = 0.75$ case are presented here. After the CH_4-air mixture is ignited, the flame anchors on top of the honeycomb and sits approximately $1.1\,mm$ downstream of the honeycomb exit. Figure 5.9 shows the contours of reaction rate and the highest reaction rate region describes the flame position. The flame position can also be observed in Figure 5.10 near $x = 0.028\,m$. In Figure 5.10, the axial variation of

mass fractions of methane, oxygen, carbon dioxide and water are also shown. The temperature can be seen to peak at $x = 0.0285\,m$ and the maximum temperature at that location is approximately $1580\,K$. The maximum temperature observed is lower than the adiabatic flame temperature because of the convective and radiative losses present in the burner system. The temperature variation inside the honeycomb can be observed in Figure 5.10 – the temperature of the incoming air-fuel mixture is approximately $1200\,K$ at the honeycomb exit location.

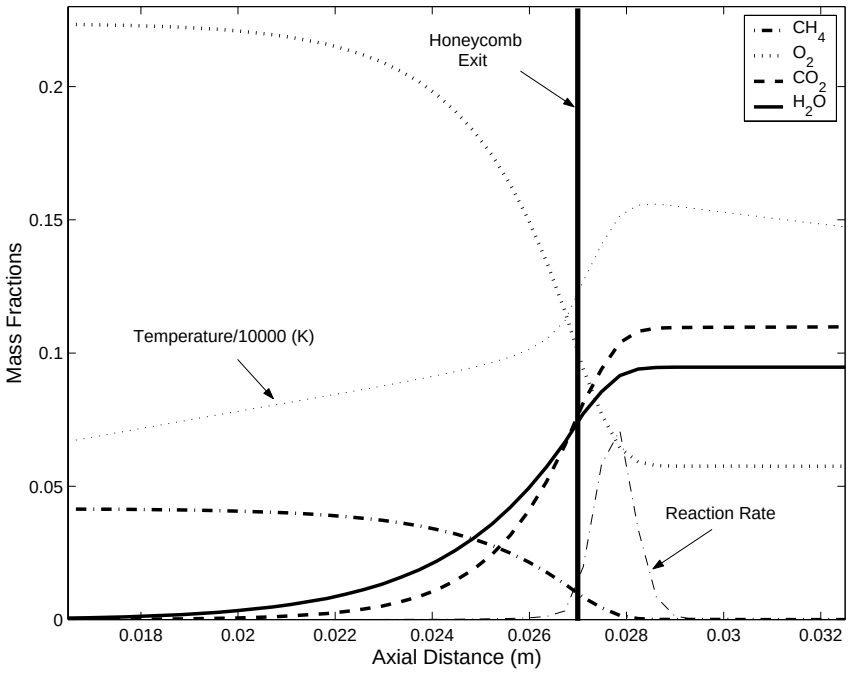

Figure 5.10: Axial variation of mass fractions of CH_4, O_2, CO_2 and H_2O inside the flat flame burner. Temperature (K) and reaction rate variations are also shown

Figure 5.11 shows the contours of temperature inside the honeycomb and in the burner section. The maximum temperature region is located immediately downstream of the honeycomb and the temperature steadily decreases downstream. The temperature is also lower near the quartz chimney wall because of convective heat losses from the outside surface of the quartz wall. Radiation plays an important role in the combustion process. The honeycomb

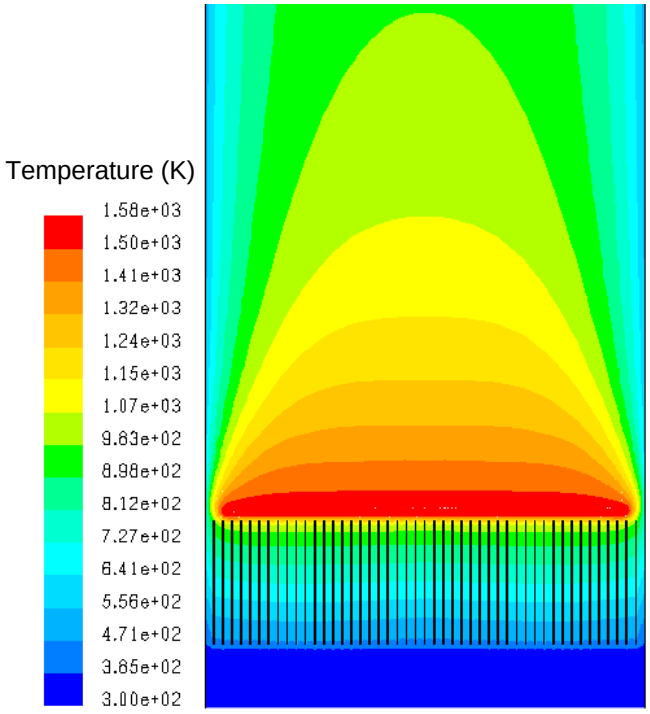

Figure 5.11: Temperature (K) contours inside the flat flame burner

top radiates heat to the quartz wall and axially outwards toward the ambient. Since hot combustion products are present downstream of the honeycomb, some part of the emitted radiation is absorbed by the products. This absorption can be observed in Figure 5.12. Near the quartz wall more radiation is absorbed because the product temperature is lower which results in higher net radiative exchange.

5.5.2 Frequency Response Function

The Frequency Response Function (FRF) between unsteady heat release rate of the laminar flat flame and the incoming mixture velocity fluctuation are described in this section. The FRF output is unsteady heat release rate (q') which has been calculated as a function of the instantaneous reaction rate (RR) integrated over the flow domain. The mean reaction rate

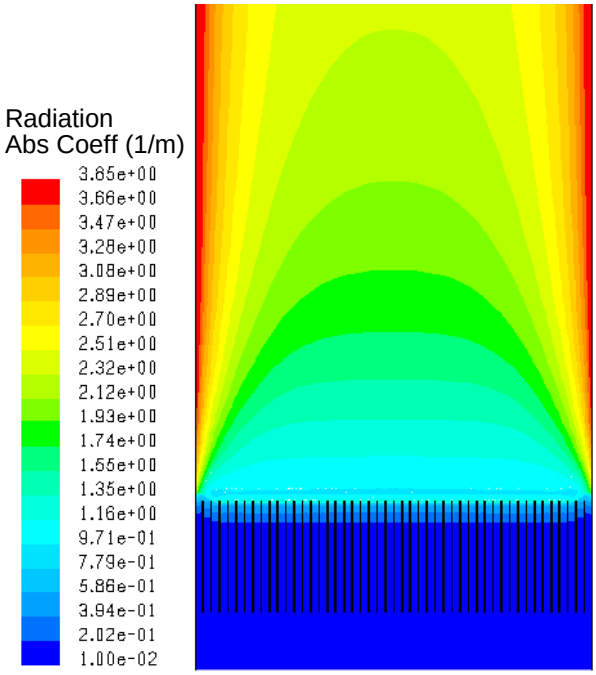

Figure 5.12: Contours of absorption coefficient $(1/m)$ inside the flat flame burner

$(\overline{RR})$ is calculated from the integrated reaction rate as:

$$\overline{RR} = \frac{\sum_{i=1}^{N} RR_i}{N} \tag{5.11}$$

where N is the number of data points collected in time t. The non-dimensional fluctuating component is then evaluated as:

$$RR'_{nd} = \frac{RR - \overline{RR}}{\overline{RR}} \tag{5.12}$$

The FRF input is velocity measured $1\,cm$ upstream of the honeycomb inlet. The velocity is non-dimensionalized using the mean value $\overline{u}$ as:

$$u'_{nd} = \frac{u - \overline{u}}{\overline{u}} \tag{5.13}$$

5.5.3 Comparison with Experimental Results

The FRF generated from the CFD simulations will be compared with FRF obtained from experimental studies [1]. In the experimental data, the input is fluctuating component of velocity (in dBV) and the output is OH^* chemiluminescence intensity (in dBV). We know from previous studies that OH^* intensity is a measure of instantaneous heat release rate from the flame [84]. Therefore, we can compare the FRF obtained from the CFD simulations with the experimentally obtained FRF. There is a scaling issue involved while comparing the magnitudes of the two FRFs. This scaling issue is present because the magnitude of the FRF calculated from the experimental data is $[I'_{OH^*}(dBV)]/[u'(dBV)]$, whereas the FRF computed from the CFD data is $[RR'_{nd}]/[u'_{nd}]$. The difference will show up in the gain (magnitude) and not in the phase plot.

Figure 5.13 shows the comparison between the FRF magnitude computed from the CFD data and the FRF magnitude obtained from experiments. The computed FRF magnitude shows a similar behavior as the experimental FRF magnitude, although the CFD model fails to capture the low frequency resonance phenomena that is observed in the experimental result. The resonance can be observed to occur around $35\,Hz$ in the experimental FRF magnitude (gain) and phase curves. The FRF phase comparison is also shown in Figure 5.13. The computed FRF phase does not follow the trend observed in the experimental FRF and shows a slope that is inverse of the experimental phase for the full frequency range of $20\,Hz$ to $300\,Hz$.

5.5.4 Observations and Recommendations

The CFD model has been able to capture part of the combustion dynamics of the flat flame, but fails to capture one important phenomenon – the low frequency resonance or the 'pulsating instability'. The 'pulsating instability' can play a role in the development of instabilities – Joulin and Clavin [70], Buckmaster [71] and Jackson and Kapila [72] have

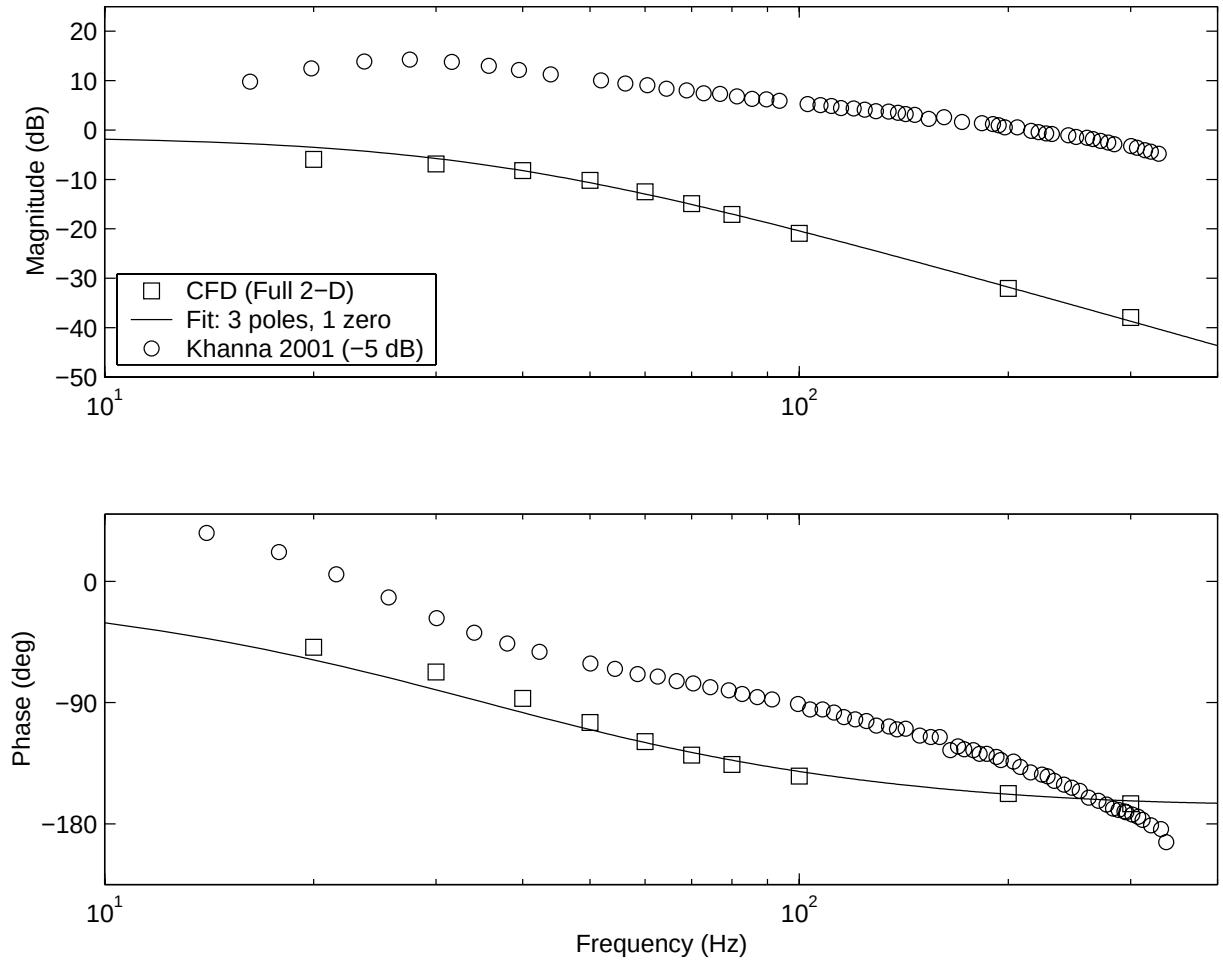

Figure 5.13: Frequency response function magnitude and phase of heat release rate due to oscillations in velocity (Full 2-D simulation, $Q = 200\,cc/s$ and $\phi = 0.75$)

shown that large enough heat losses can make premixed flames unstable to the pulsating instability. It is, therefore, important that the low frequency resonance be captured by the CFD model and a physical explanation be proposed for the causes behind the phenomenon.

To investigate the causes behind the CFD model's failure and to improve the model further, we need to consider several factors that affect the model's performance: grid resolution, boundary conditions, heat transfer modeling. We can safely assume that the two-step chemical mechanism implemented in the model is a good choice since the resonance occurs at a low frequency and comparatively chemical time scales are several orders of magnitude smaller ($O[1 \times 10^{-3}\, s]$). The reaction rate, which is the indicator of heat release rate, is dependent on the flat flame area change due to incoming velocity fluctuations (in effect a variation in laminar flame speed, S_L). The incoming acoustic wave (resulting from u') must be incident on a 'perfect' flat flame. A 'perfect' flat flame can be characterized by perfectly parallel iso-contours of reaction rate. Although, the flame looks flat in Figure 5.9, a closer look at the iso-contours of reaction rate in Figure 5.14 shows that the flame is not absolutely flat. The innermost region of the flame is characterized by the highest reaction rate, but these regions are confined to the immediate downstream regions of the honeycomb fluid paths. They are not present downstream of the honeycomb solid regions, as can be observed in Figure 5.14.

Several grid adaptations were performed on the original coarse grid before flow forcing was initiated. Parameters like flame thickness, integrated reaction rate, axial distribution of species mass fraction and temperature profile were employed to assess the effect of grid adaptation. It was found out that the grid finally obtained was fine enough to capture the steady state characteristics of the flat flame. Since, the final aim is to compare the CFD model FRF with experimental results, the correct parameter that should be used in grid adaptation is the final form of the FRF itself. Using FRF as the parameter means considering several runs of the code to achieve the desired grid resolution. Therefore, FRF as a parameter is computationally prohibitively expensive to implement. As it is difficult to isolate one variable which is responsible for the CFD model's failure, blaming grid adaptation

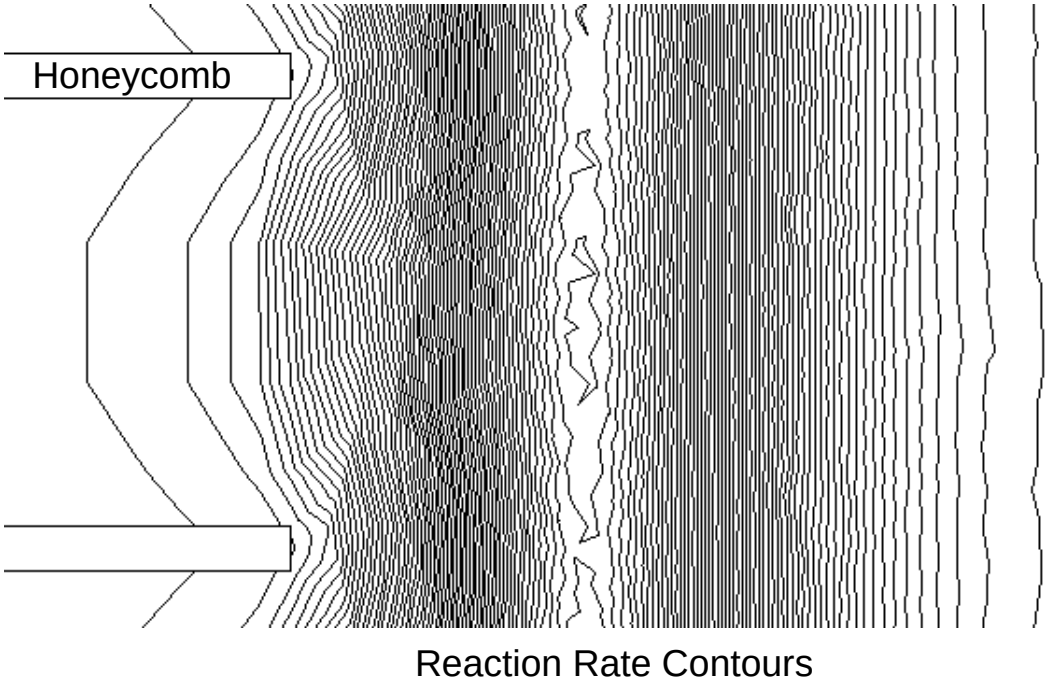

Figure 5.14: Closeup of reaction rate iso-contours at the immediate downstream of the honeycomb channels

alone will probably not be the right approach.

A simplified method of investigation that can be applied is to study the flat flame downstream of a single channel of the honeycomb. This attempt is possible if the relevant fluid dynamic and heat transfer processes for the flat flame combustion environment are understood sufficiently. The effect of convective heat losses from the quartz duct outer wall can be ignored if the center most honeycomb channel is considered. Similarly, the effect of specular reflection on the quartz wall can also be ignored since quartz transmits thermal radiation for wavelengths less than $4\,\mu m$ (wavelength region of interest in this study is $\lambda < 4.5\,\mu m$), paving the way to using a simpler (and computationally less expensive) radiation model. Another advantage of working with the single channel geometry is the excellent grid resolution that will be possible in the flame region.

Another area of concern is in the accuracy of boundary conditions implemented in the full

two-dimensional investigation. The inlet boundary condition ensures a sinusoidally varying velocity. An improved implementation of the inlet boundary condition in FLUENT is the mass-flux inlet condition. The mass-flux inlet condition is implemented and its relative advantages are highlighted in the next chapter.